Breast Cancer Research

RESEARCH

Open Access

Modelling the metastatic immune microenvironment in triple-negative breast cancer

Laura Rodriguez de la Fuente[1,2,3], Andrew M. K. Law[3], Laura Rangel-Sanchez[1,3], Jeron Venhuizen[3], Fiona Steffan[3], Lesley Castillo[3], Robin L. Anderson[4,5,6], Fatima Valdes-Mora[1,2,3,7*†] and David Gallego-Ortega[1,3,7*†]

Abstract

Background This study uses the well-established 4T1.2 and 67NR mammary cancer cell lines as syngeneic immunocompetent implantable murine models of triple negative breast cancer.

Methods Using pair-wise analysis, we compare the implantation route of cancer cells by conventional orthotopic injections in the mammary fat pad vs intraductal injection in the mammary ductal tree. We reveal that implantation methodology influences the inherent metastatic potential, tumour progression and the co-evolution of cancer cells and the tumour microenvironment.

Results Intraductal injection accelerates tumour growth, especially in the non-metastatic 67NR model, and better mimics early tumourigenic events that preserve the tissue microenvironment crucial for tumour-stromal interactions. Immune cell composition differences are driven by the tumour model but independent of the implantation method, however, intraductal implantation carries higher stromal proportions at early stages of tumour development. In the 4T1.2 model, intraductal injection increases metastatic burden. We found markedly different systemic inflammation traits unique to the metastatic 4T1.2 scenario consistent with the acquisition of a cancer immunotolerant phenotype during progression to metastatic disease. Metastatic dissemination induced a myeloid-dominated inflammatory milieu, particularly driven by granulocytic myeloid-derived suppressor cells, contrasting with the lymphocyte-rich profile in the non-metastatic 67NR tumours. Immune responses of the metastatic 4T1.2 scenario were further analysed by targeted single-cell RNA sequencing revealing distinct immune activation in primary tumours, emphasising the differential role of immune cells between primary and metastatic lesions.

Conclusions Our findings stress the importance of carefully selecting experimental models to faithfully recapitulate breast cancer progression and metastasis, providing insights for future therapeutic interventions focused on immune modulation.

†Fatima Valdes-Mora and David Gallego-Ortega contributed equally as last authors.

*Correspondence:
Fatima Valdes-Mora
fvaldesmora@ccia.org.au
David Gallego-Ortega
David.GallegoOrtega@uts.edu.au

Full list of author information is available at the end of the article

Keywords Triple negative breast cancer, 4T1.2, MIND, Lung metastasis, Pre-clinical mouse models, Myeloid-derived suppressor cells, Tumour and metastatic immune microenvironment

Background

Breast cancer (BCa) is the most common cancer among women, with over 2.3 million new cases globally in 2020 [1] and the fifth leading cause of cancer-related death [2]. Understanding the intricate dynamics of tumour growth and progression in BCa is imperative for devising effective therapeutic strategies. The choice of experimental models has a pivotal role in ensuring the reliability and translatability of research findings to clinical settings, particularly considering the co-evolution of cancer cells and the tumour ecosystem, and the recapitulation of the influence of immune cell populations on BCa progression.

Triple negative breast cancer (TNBC) is the most immunogenic subtype of BCa. It comprises 10–15% of all breast cancer cases and shows the poorest prognosis [3]. Adjuvant or neoadjuvant chemotherapy has been the mainstream treatment for TNBC, achieving responses ranging 40–50% depending on the clinical setting [4–6]. In recent years, the role of tumour-infiltrating immune cells in regulating BCa progression and therapeutic response has attracted significant attention [7–14]. Elevated levels of tumour-infiltrating CD8 + cytotoxic T lymphocytes correlate with a more favourable prognosis [15], whereas regulatory T cells (Tregs), tumour-associated macrophages (TAMs), and myeloid-derived suppressor cells (MDSCs) are associated with poorer chemotherapy response and overall survival [16–18]. Due to the heightened immunogenicity of TNBC, immunotherapy with checkpoint inhibitors in combination with chemotherapy increased therapeutic responses compared with chemotherapy alone [4, 19, 20]. However, the efficacy of immunotherapy is still limited to a subset of patients [19, 21–23]. The limited therapeutic success in TNBC is caused not only by the intrinsic heterogeneity of the cancer cells but also by the cancer-associated cells within the tumour microenvironment (TME) that confer immunotolerance and resistance to cancer therapy [21, 22].

Syngeneic models have been instrumental in elucidating the interplay between the immune system, tumorigenesis and metastasis, including the discovery of novel anti-cancer treatments such as immunotherapy [24]. However, modelling breast cancer with allograft implantation of cancer cells may not accurately reflect the multistep process of tumorigenesis, including the co-evolution of cancer cells and key aspects of their surrounding microenvironment such as the extracellular matrix (ECM). The choice of implantation method significantly impacts the translatability of these models [25–27]. For instance, subcutaneous implantation fails to preserve the endogenous tumour microenvironment leading to decreased lymphoid cell infiltration, reduced vascular density and limited interaction of cancer cells with the ECM [28–31]. Additionally, subcutaneous tumours exhibit altered drug distribution [31] and reduced invasive and metastatic properties [30]. In contrast, orthotopic fat pad implantation has been shown to provide a more physiologically relevant model, characterised by increased tumour vasculature, malignant features and metastatic potential compared to subcutaneously implanted cells [27]. However, conventional orthotopic fat pad implantation methods also may not fully recapitulate the sequential progression of cancer stages. To address this limitation, the mammary intraductal (MIND) method has been developed to better mimic the natural disease progression and metastatic dissemination [26, 32–37].

In this study, we investigated the comparative outcomes of two BCa implantation methods: the conventional orthotopic fat pad inoculation of cancer cells in the mammary fat pad and the intraductal injection of cancer cells via the inguinal teat. For both methods, we utilise the highly metastatic (4T1.2) and non-metastatic (67NR) murine mammary tumour lines. In the conventional orthotopic fat pad method, cancer cells are inoculated within the mammary fat pad, and in the intraductal model, cells are introduced through the teat directly into the mammary ducts. By implanting the cancer cells into the appropriate histological location within the epithelial ductal tree, we propose that intraductal implantation is an enhanced model to study cell-to-cell and cell-to-ECM communication within the tumour microenvironment (particularly at early stages) during breast cancer growth and metastasis. This intraductal modality serves as a foundation for high-resolution studies that will assist in the identification and design of novel anti-cancer approaches to target the tumour ecosystem, including immunotherapy.

Through a comprehensive examination encompassing tumour kinetics, histological morphology, immune responses and metastatic dissemination, we aim to elucidate the most suitable model for studying BCa progression and metastasis. We also provide a high-resolution functional atlas of the immune components in mammary tumours and during the establishment of lung metastasis in the 4T1.2 TNBC model. Collectively, our findings underscore the importance of experimental model selection and route of cancer cell implantation technique to faithfully recapitulate the intricacies of BCa progression and metastasis. Our study lays the foundation for further

mechanistic studies and is poised to become a valuable resource in identifying and designing innovative anti-cancer immunotherapy strategies.

Methods

Ethics statement

Animals were housed within the Biological Testing Facility of the Garvan Institute of Medical Research and approved under the St. Vincent's Hospital Animal Ethics Committee (AEC) #17/23 and #19/02. Immunocompetent BALB/c were maintained in pathogen-free housing with food and water provided ad libitum in a 12:12 h light–dark cycle. All surgical procedures were performed under anaesthetic with 1L/minute of oxygen and 5% Isoflurane for induction and 1L/minute of oxygen and 2% Isoflurane for management. The mice were placed in a room temperature recovery box post-surgery with "half on/half off" over a warm heat pad. All animals received analgesia after surgery. The following day, the animals were checked for general well-being. Animals were then monitored twice weekly, and tumour measurements were made using electronic callipers. Ethical endpoint was defined by any tumour diagonal higher or equal to 1.1 cm or 10% of tumour to body weight. At collection time or endpoint, mice were euthanised with CO2 asphyxiation followed by cervical dislocation.

Cell culture

The isogenic breast cancer cell lines 4T1.2 (highly metastatic) and 67NR (non-metastatic) were derived from the same spontaneous mammary tumour within BALB/c [38] and were further developed and characterised [39, 40]. The 4T1.2 is a single cell clone that readily metastasises to lung and bone and is derived from the original 4T1 cell line [40]. Both 4T1.2 and 67NR cell lines used in this study were tagged with a vector encoding a mCherry fluorescent protein. Cells were cultured in MEM alpha medium (Gibco/Life Technologies, VIC, Australia, Cat# 12,571,063) supplemented with 5% FBS (GE Healthcare, NSW, Australia, Cat# SH30406.02) and were maintained at 37 °C with 5% CO2. Mycoplasma was screened in cell culture to ensure that cells were free from contamination. At 80% confluence, cells were trypsinised for 3 min. Trypsin was neutralised with MEM Alpha medium with 5% FBS, and cell numbers were counted manually under a light microscope. The calculated number of cells that were required were aliquoted and pelleted through centrifugation at 1200 rpm for 5 min at 4 °C. The supernatant was removed, and the cells were resuspended in PBS to the required concentration for injection (Gibco/Life Technologies, VIC, Australia, Cat# 14,190-250).

Animal models

Female BALB/c mice aged 7–8 weeks were purchased from the Australian BioResources (MossVale, NSW, Australia). Mice were allocated into different experimental groups based on the method of injection (conventional fat pad or intraductal cell inoculation) and were inoculated with either 5×10^4 4T1.2 cells or 2×10^4 67NR cells.

Conventional orthotopic fat pad injection

Animals were anaesthetised with Isoflurane and the lower abdomen was sterilised with an ethanol wipe. A "Y" shaped incision was made along the lower abdominal midline and toward the back leg. The skin was lifted to reveal the fourth inguinal mammary fat pad, where 100uL of the cell suspension was injected with a 25-gauge 5/8″ syringe. The incision was then sealed using surgical wound clips, and the animal was placed in the recovery box. Animals were monitored twice weekly, and surgical clips were removed ten days after surgery.

Intraductal injection

MIND injections were performed as previously described [32] but modified without a "Y" shaped incision in the abdomen. Briefly, animals were anaesthetised with Isoflurane, and the area around the nipple of the fourth inguinal mammary gland was carefully shaved and sterilised with an ethanol wipe. The tip of the teat of the 4th inguinal mammary gland was removed using 3 mm cutting-edge Vannas Spring Scissors (F.S.T, CA, USA, Cat# 15,000–00). The area of the cut was stained with a drop of 0.4% Trypan Blue (TP) solution to visualise the opening of the primary duct. Prior to injection, cell suspensions are mixed with TP at a concentration of 1:4 of TP to cell suspension ratio to observe the injection. 4 µL of the cell suspension was injected through the ductal opening via a Hamilton syringe with a 30-gauge blunt-ended fixed 1/2-inch needle. Successful injections were indicated by the blue dye entering through the entire ductal tree (Fig. 1A). Animals were placed in a recovery box and consistently monitored weekly post-surgery until tumours were collected.

Tissue digestion

Tissues were digested as previously described [41]. Briefly, samples were enzymatically digested with 15,000U collagenase (Sigma, NSW, Australia, Cat# C9891) and 5000U hyaluronidase (Sigma, NSW, Australia, Cat# H3506) in DMEM medium (Gibco/Life Technologies, VIC, Australia, Cat# 11,995-073) at 37 °C for 1 h at 200 rpm in a shaking incubator. The samples were then further incubated in 2.5% trypsin (Gibco/Life Technologies, VIC, Australia, Cat# 15,090,046) with 1 mM EGTA (Sigma, NSW, Australia, Cat# E3889-100G) in PBS for 1 min in a 37 °C water bath. Each sample was

individually resuspended with a P1000 Gilson Pipette constantly throughout the trypsin digestion. Spleens were disaggregated through a 40 μM cell strainer with the end of a 10 mL plastic syringe and collected in 2% FBS in PBS. Red blood cells were lysed with 155 mM ammonium chloride (Sigma, NSW, Australia, Cat# 213,330-500G) for 5 min in a 37 °C water bath, and the sample was filtered through a 40 μM filter.

Blood collection

Peripheral blood was collected from anaesthetised mice via a cardiac puncture. Blood samples were mixed with heparin and were washed three times with 2% FBS in PBS. Red blood cells were lysed with 155 mM ammonium chloride for 10 min in a 37 °C water bath.

Flow cytometry

Cells were blocked with 6.25 μg/mL of Mouse BD Fc Block™ (BD Biosciences, CA, USA, Cat# 553,141) and 2.3 μg/mL of Rat Gamma Globulin (Jackson ImmunoResearch Laboratories Inc., PA, USA, Cat# 012–000-002) in 2% FBS in PBS for 15 min on ice prior to antibody staining. Antibody staining was performed for 30 min on ice in the dark with the following antibodies: 1:400 CD45 (Clone 30-F11), 1:400 CD11b (Clone M1/70), 1:200 F4/80 (Clone BM8), 1:200 Ly6C (Clone HK1.4), 1:200 Ly6G (Clone 1A8), 1:100 CD3 (Clone 17A2), 1:100 CD4 (Clone GK1.5), 1:100 CD8 (Clone 53–6.7), 1:100 B220 (Clone RA3-6B2). BD CompBead™ were used for isotype controls for all antibodies. Single-cell suspensions from tumours were used as compensation for mCherry as both murine cell lines, 4T1.2 and 67NR have been infected with the mCherry fluorescent reporter. Flow cytometry was performed using the BD FACS Symphony™ (BD Biosciences, CA, USA) acquiring equivalent number of events, and analysis was performed with the BD FACS Diva™ software and exported for further analysis with FlowJo (Treestar Inc., OR, USA). Gating strategy was followed as previously described [42], and outlined in Supp. Fig. 1 with representative analysis.

Immunohistochemistry

The tumour and lungs were fixed in 10% neutral buffered formalin overnight. Formalin-fixed paraffin-embedded (FFPE) samples were cut into 4 μm sections using a Leica RM2235 microtome (Leica Biosystems, Wetzlar, Germany) and were incubated on a Superfrost plus slide for 2 h in a 60 °C oven for maximum adhesion. For staining, all slides were deparaffinised before following separate protocols for H&E, Ki67, cleaved caspase-3 (CC3), and picrosirius red staining. Antibody-based staining was performed on a Leica Bond RX (Leica Biosystems, Wetzlar, Germany) using the Ki67 antibody (Thermo Scientific, NSW, Australia, Cat# RM-9106-S1, 1:500 dilution), CC3 antibody (Cell Signaling, MA, USA, Cat# 9661, 1:500 dilution), HIF-1 (Novus Biologicals, Cat# NB100-449, 1:400 dilution), GLUT-1 (Abcam, Cat# AB115730, 1:1000 dilution)—HIER1-20 min 100 degrees. The staining protocol was performed using the manufacturer's Bond Polymer Refine IHC protocol (no haematoxylin) with a 60-min antibody staining. Slides were counterstained with Haematoxylin following the protocol from the Shandon Instant Hematoxylin Kit, and cover slipped. H&E staining was performed following a standardised protocol, and cover slipped. Slides stained for picrosirius red were first stained in Haematoxylin for 30 s before treatment with 0.2% (w/v) aqueous phosphomolybdic acid for 2 min at room temperature. Picrosirius red solution was made by dissolving Direct Red 80 with a saturated picric acid solution, and the slides were stained with picrosirius red solution for 1 h. Excess picrosirius red solution was washed off the slides for 2 min with acidified water made from 0.5% acetic acid in distilled water and submerged in 70% ethanol for 1 min. The slides were dehydrated, and cover slipped. Sections were photographed with a Leica DM4000 light microscope under a 10X objective lens. All images were quantified using Andy's Algorithm, a series of automated image analysis pipelines in FIJI [43].

QuPath quantification of immunohistochemical staining

Whole tissue slides were scanned at 20 × using a Zeiss Axioscan Z1 with the brightfield setting at 20x. QuPath was used to assess the tumoral i nvasive areas. Briefly, 20–30 ROIs from different tissues were used for pixel training classification to assess the stromal, cancer and invasive regions. The following parameters were used: R-trees, 7.04 μm/px resolution, channels: Green, Red, Hematoxylin, Scales (1, 4) and 2 Features. For GLUT1-positive staining, tissue boundaries were determined using the following parameters: DAB channel, threshold of 0.25, and sigma of 0.2 AT 3.52 μm/px resolution. A threshold of 0.68 was used to analyse the areas with a strong GLUT1 signal.

Immunofluorescence

For immunofluorescence analyses, FFPE Sects. (4 μm) were pre-processed using a Leica BOND RX autostainer. Tissues were then washed and permeabilised with 0.3% Triton for 20 min. Labelling with primary antibodies was performed in blocking buffer of 3% BSA. Antibodies used were anti-alpha SMA (Abcam, Cat# ab124964, 1:500 dilution), and anti-PanCK (Abcam, Cat# AB86734, 1:100 dilution). AlexaFluor-555/ 647-conjugated secondary antibodies (Thermo Fisher Scientific, 1:400 dilution) were used to detect positive signals. Sections were counterstained with DAPI (Thermo Fisher Scientific) before mounting with ProlongGold mounting medium. Images

were acquired using a Leica Stellaris SP8 confocal system with a 20 × objective.

Statistical analysis

Statistical analyses were made using the software GraphPad Prism 8 or with Python using the Seaborn library. All data are expressed as the mean with error bars corresponding to the standard error (SEM) or standard deviation (SD). Statistical significance between groups was calculated using an unpaired student's t-test or one-way Anova and post hoc Tukey test.

Single cell RNAseq analysis

Tumours and lungs from three mice of the 4T1.2 intraductal model were recovered 3.5–4 weeks after tumour implantation and dissociated to single-cell suspensions as described [41]. Cell suspensions from the three mice were pooled by organ and sorted on a FACS Aria III using the pan leukocyte CD45 marker and DAPI for dead cell exclusion. Viably sorted leukocytes were immediately captured and barcoded for single-cell RNAseq using the BD Rhapsody platform and the targeted immune response panel following the manufacturer's instructions. The resulting libraries were sequenced in a Novaseq 6000 instrument following BD recommendations.

Fastq files were subsequently uploaded into Seven Bridges (BD Biosciences) for barcode demultiplexing, alignment of reads to the mm10 murine genome and quantification of UMIs and genes per cell. The resulting data frame was used as input for the downstream analysis of the R package Seurat V4 [44]. The gene expression data were normalized using the SCT transform normalization algorithm. Dimensional reduction of the dataset was performed by using principal component analysis (PCA) and Uniform Manifold Approximation and Projection (UMAP). Unsupervised clusters were determined using the Louvain algorithm, according to the instructions in Seurat. Cell identities were annotated using the SingleR package [45] based on the mouse cell type reference generated by the Immunologic Genome Project [46]. Differential gene expression was evaluated with the *FindAllMarkers()* and the following parameters: logfc.threshold = 0.25, test.use = "wilcox", min.pct = 0.1.

Results

Tumour growth kinetics differ between BCa implantation routes and mouse models

The co-evolution and interactions of cancer cells and immune cell lineages within the TME are critical to identifying the key cellular players and molecular mechanisms

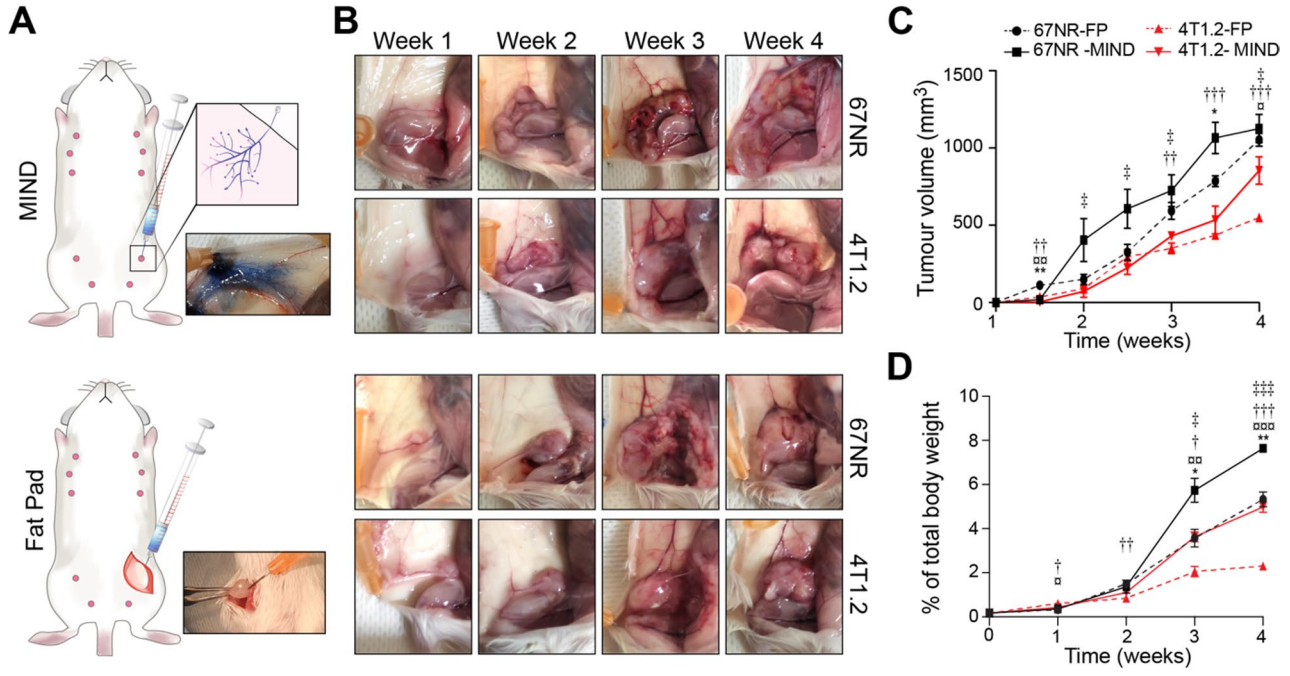

Fig. 1 Comparison of tumour growth and tumour weight between 4T1.2 and 67NR models in conventional orthotopic fat pad and MIND injection modalities. **A** Schematic of intraductal and fat pad injections **B** Representative images of primary tumours at indicated weeks after cell injection. **C** Growth kinetics of 4T1 (red) and 67NR (black) tumours injected intraductally (solid line) or through the fat pad (dashed line), volume calculated as V = (Dxd2)/2. **D** Tumour weights of animals harvested over 4 weeks represented as the percentage of total body weight. All statistical tests were performed with a student's t-test with at least n = 3 replicates per group. * = significance between 67NR fat pad and 67NR MIND; ¤ = significance between 4T1.2 fat pad and 4T1.2 MIND; † = significance between 67NR fat pad and 4T1.2 fat pad ‡ = significance between 67NR MIND and 4T1.2 MIND need for p values ($p < 0.05$, $p < 0.01$, $p < 0.001$)

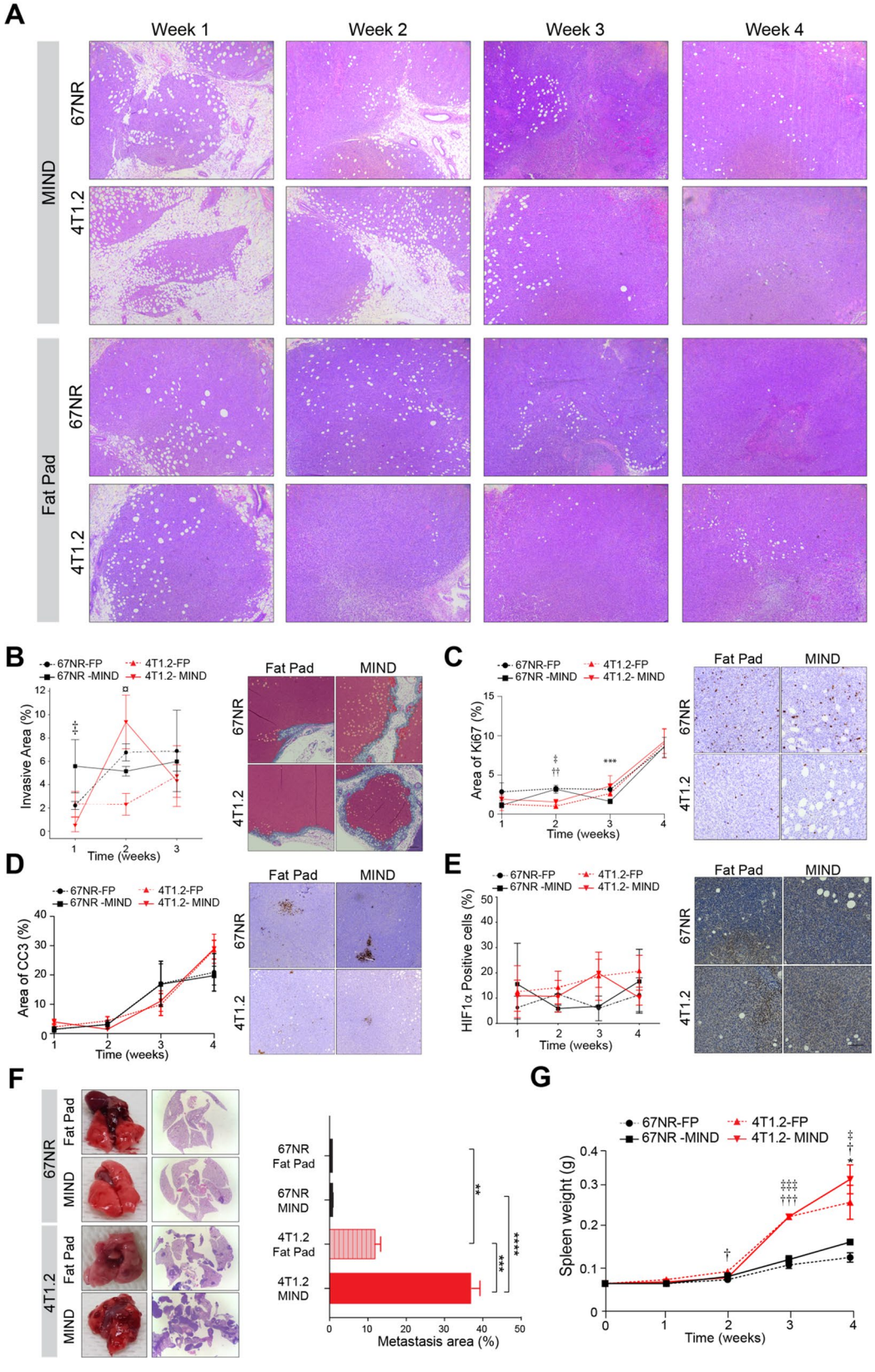

Fig. 2 (See legend on next page.)

(See figure on previous page.)

Fig. 2 Histopathological and metastatic burden comparison of tumour progression between conventional fat pad and MIND injection. **A** Representative H&E photomicrographs of harvested primary tumours over 4 weeks. **B** left) Quantification over 3 weeks of the area of the invasive edge. **B** right) Representative images of the 2-week timepoint showing tumour masses (pink) and invasive edge (cyan). **C**–**E**) Quantification over 4 weeks and representative IHC at 2 weeks of **C** Ki67; **D** Cleaved caspase-3; and **E** HIF1-α. **F** left) Representative images and H&E of lungs at 4 weeks post-injection. **F** right) Histogram showing the area of metastasis in the lungs at week 4. **G** Mean spleen weights at the indicated times. All statistical tests were performed with a Student's t-test with at least n = 3 replicates per group. * = significance between 67NR orthotopic and 67NR intraductal; ¤ = significance between 4T1.2 orthotopic and 4T1.2 MIND; † = significance between 67NR orthotopic and 4T1.2 orthotopic; ‡ = significance between 67NR MIND and 4T1.2 MIND ($p < 0.05$, $p < 0.01$, $p < 0.001$)

that promote immune tolerance and contribute to metastatic dissemination. To find the optimal model for studying the co-evolution of the immune system and cancer cells during metastasis, we first characterised two methods of cancer cell injection, conventional orthotopic fat pad and intraductal implantation (MIND) (Fig. 1A). We took a comparative approach using the metastatic 4T1.2 and the non-metastatic 67NR murine mammary tumours. Tumours in both mouse models were palpable one week post-injection and grew over time (Fig. 1B). Intraductal tumours showed faster growth kinetics compared to fat pad-injected tumours (Fig. 1C). In addition, 67NR tumours consistently developed more rapidly, reaching a higher tumour volume regardless of the injection method, which was consistent with higher tumour weight at harvest (Fig. 1D). The higher rate of 67NR tumour growth might relate to a further evolution and/or the passage number of the cell line compared with previous reports [47]. These results demonstrate the different patterns and rates of tumour development depending on the method used to implant BCa cells and the model used (metastatic or non-metastatic). The MIND technique demonstrated an accelerated growth rate compared to conventional orthotopic fat pad implantation, with the non-metastatic 67NR mouse model reaching higher tumour volumes from week 2 post-cancer cell injection.

Intraductal injection better recapitulates the course of BCa progression

We next analysed tumour histology by H&E at weekly intervals over four weeks (Fig. 2A). Histological analysis of the MIND implanted tumours both in the 4T1.2 and 67NR models revealed a multifocal formation of tumours at the first week post-implantation with abnormal formations of epithelial cells around mammary ducts. The continuous growth and invasion of cancer cells throughout the mammary gland continued in week 2, as areas of the tumour converged together (Fig. 2A, top), suggesting a continuous dynamic interaction with the surrounding stroma. By weeks 3 and 4, the mammary gland was completely invaded with foci of cancer cells. On the other hand, in the fat pad model, the injection site was already composed primarily of a single mass of cells from week 1 (Fig. 2A, bottom). By week 3, both MIND and fat pad models were similar at the histological level. To illustrate the increased potential for tumour stroma-interactions in the intraductal model, we performed a comparative analysis of the invasive tumour edge identified through a machine training algorithm (QuPath) (Supp. Fig. 2A). Both intraductal models showed a significantly higher proportion of invasive edge area at early stages of tumour development (week 1 for 67NR and week 2 for 4T1.2 tumours). These results suggest that the engraftment of the tumours in the fat pad bypasses the key initial steps of tumour progression and potential cell-to-cell interactions between cancer cells, the mammary ductal epithelium, and the mammary stroma.

Markers of proliferation (Ki67), apoptosis (cleaved caspase 3, CC3) and fibrillar collagen organisation (Picrosirius) were assessed in primary tumours resected over the 4 weeks. All models showed a constant and similar proliferation rate up to week 3, dramatically increasing the proportion of Ki67 + cells at week 4 (Fig. 2C). Likewise, the trend of CC3 + cells was similar between models and injection modalities, constantly increasing from week 2 and reaching a peak at week 4 post-injection (Fig. 2D). Finally, analysis of picrosirius staining showed no statistical difference in the collagen organisation during tumour development among the four conditions (Supp. Fig. 2B–C).

Given the different focal nature of tumour formation in the intraductal and fat pad models, we investigated the development of hypoxia during tumour growth using immunohistochemistry (IHC) staining of the canonical hypoxia markers HIF-1α and GLUT-1 [48]. Our analysis showed that the area of tumour HIF-1α staining was not significantly different between intraductal and fat pad tumours, even at early timepoints (Fig. 2E, Supp. Fig. 4A–B), however the extent of hypoxia correlated with tumour size in both models and both tumour types (Supp. Fig 3C). Consistent with hypoxic regions, adjacent tissue sections stained with CC3, Ki67, and GLUT-1 revealed a high density of CC3 but not Ki67 in GLUT-1-positive areas, suggesting a link between hypoxic regions and apoptosis (Supp. Fig. 3A).

The crosstalk between cancer cells and the surrounding TME components is key for metastatic dissemination [49]. To determine whether the route of implantation impacted metastatic burden, metastatic lung lesions were quantified at 4 weeks by histopathology [43] (Fig. 2F). As expected, our analysis shows that 67NR cells did not develop metastasis regardless of the

route of implantation. However, we observed a significant increase in the metastatic burden in the MIND-injected 4T1.2 model compared to the fat pad injection, where metastases covered a large proportion of the lung area (Fig. 2F, right). These results suggest that the cell-to-cell interactions occurring between intraductally injected cancer cells and the surrounding mammary gland and increased surface access of cancer cells are potentially relevant to fostering metastatic dissemination.

Metastatic dissemination is often facilitated by immunosuppressive cells that induce tumour tolerance and pre-metastatic niche formation [42, 50, 51]. To monitor the inflammation associated with metastatic dissemination, we assessed the development of splenomegaly – a condition frequently linked with systemic inflammatory responses such as those seen in metastatic cancers [51, 52]. We monitored the weight of the spleens at weekly intervals. Our analysis shows that 4T1.2 associated spleens were larger than those of 67NR from week 3 post-implantation, independent of the implantation route (Fig. 2G). These data indicate that the metastatic 4T1.2 model promoted a greater inflammatory response than 67NR tumours.

Collectively, these results show that the intraductal modality represents the mechanisms of tumorigenesis and cancer progression more accurately than occurs via fat pad injection.

Intraductal cell implantation maintains a higher proportion of stroma but similar immune composition at early stages of tumour development

To understand the impact that the implantation route has on the cellular composition of 4T1.2 and 67NR tumours, we quantified the proportions of the main cellular compartments (cancer, stroma and immune) using flow cytometry. Our analysis showed that out of the live (DAPI negative cells), the proportion of cancer cells (CD45−/ mCherry+) in the intraductal model was lower compared to the fat pad models during the first week post-implantation (Fig. 3A). When comparing cellular models, and in line with previous results, the 67NR model showed a significantly higher proportion of cancer cells than the 4T1.2 model from week 3 (Fig. 3A). Consistent with the lower number of tumour cells, intraductally implanted tumours had a higher proportion of stromal cells (CD45-/ mCherry-) than fat pad-implanted tumours at week 1 (Fig. 3B). To further characterise the stroma at this tumour development stage, we analysed the content of αSMA, a canonical marker of fibroblasts, in immunofluorescence analysis compared to PanCK to identify tumour areas (Supp. Fig. 4A). Consistent with the flow cytometry results, MIND tumours presented a higher representation of fibroblasts compared to the fat pad model in both cell lines (Supp. Fig. 4B). From week 2, the implantation route did not have any impact on the proportion of stromal and cancer cells. The immune infiltration in tumours was higher in the metastatic 4T1.2 model than in the 67NR model (Fig. 3C). However, this increase in tumour-infiltrated immune cells was independent of the route of cancer cell implantation.

We next evaluated the composition of the main immune cell lineages infiltrated into tumours (Fig. 3D–H). All four models showed similar trends of immune infiltration over the four weeks. Monocytes (CD45 + / CD11b + / Ly6C +) proportions remained similar over 3 weeks (Fig. 3D). However, at 4 weeks, monocytes in the

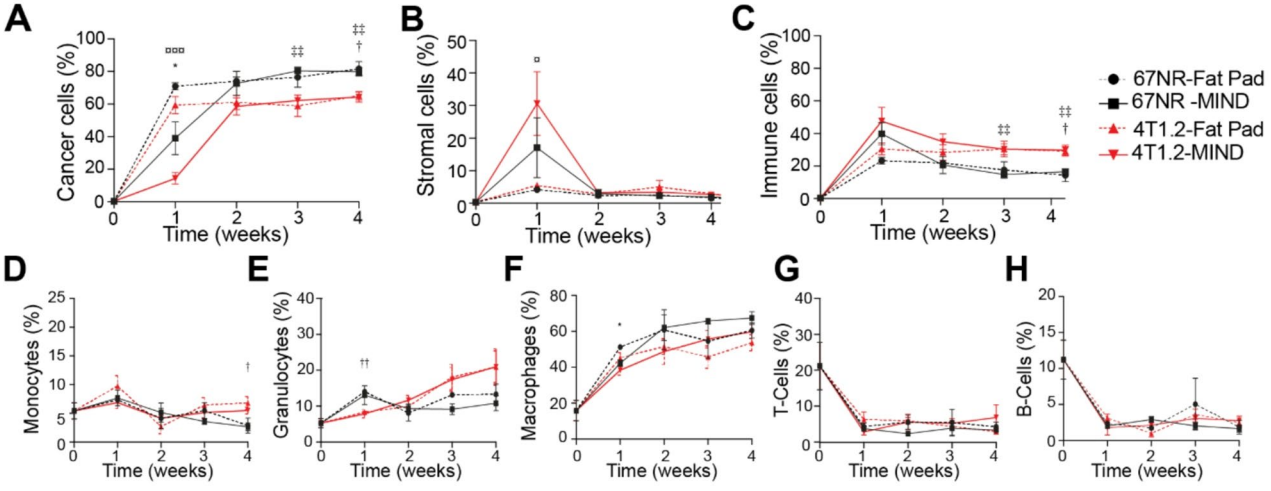

Fig. 3 Characterisation of the cellular composition of fat pad and MIND 4T1.2 and 67NR tumours. Relative proportions of all live cells of **A** cancer, **B** stromal, and **C** immune cells over 4 weeks post-implantation. Immune tumour infiltration over 4 weeks of **D** monocytes, **E** granulocytes, **F** Macrophages, **G** T-cells and **H** B-Cells. Proportions in **D**–**H** are relative to all immune cells. All statistical tests were performed with a student's t-test with at least n = 3 replicates per group. * = significance between 67NR fat pad and 67NR MIND; ¤ = significance between 4T1.2 fat pad and 4T1.2 MIND; † = significance between 67NR fat pad and 4T1.2 fat pad; ‡ = significance between 67NR MIND and 4T1.2 MIND. ($p < 0.05$, $p < 0.01$, $p < 0.001$)

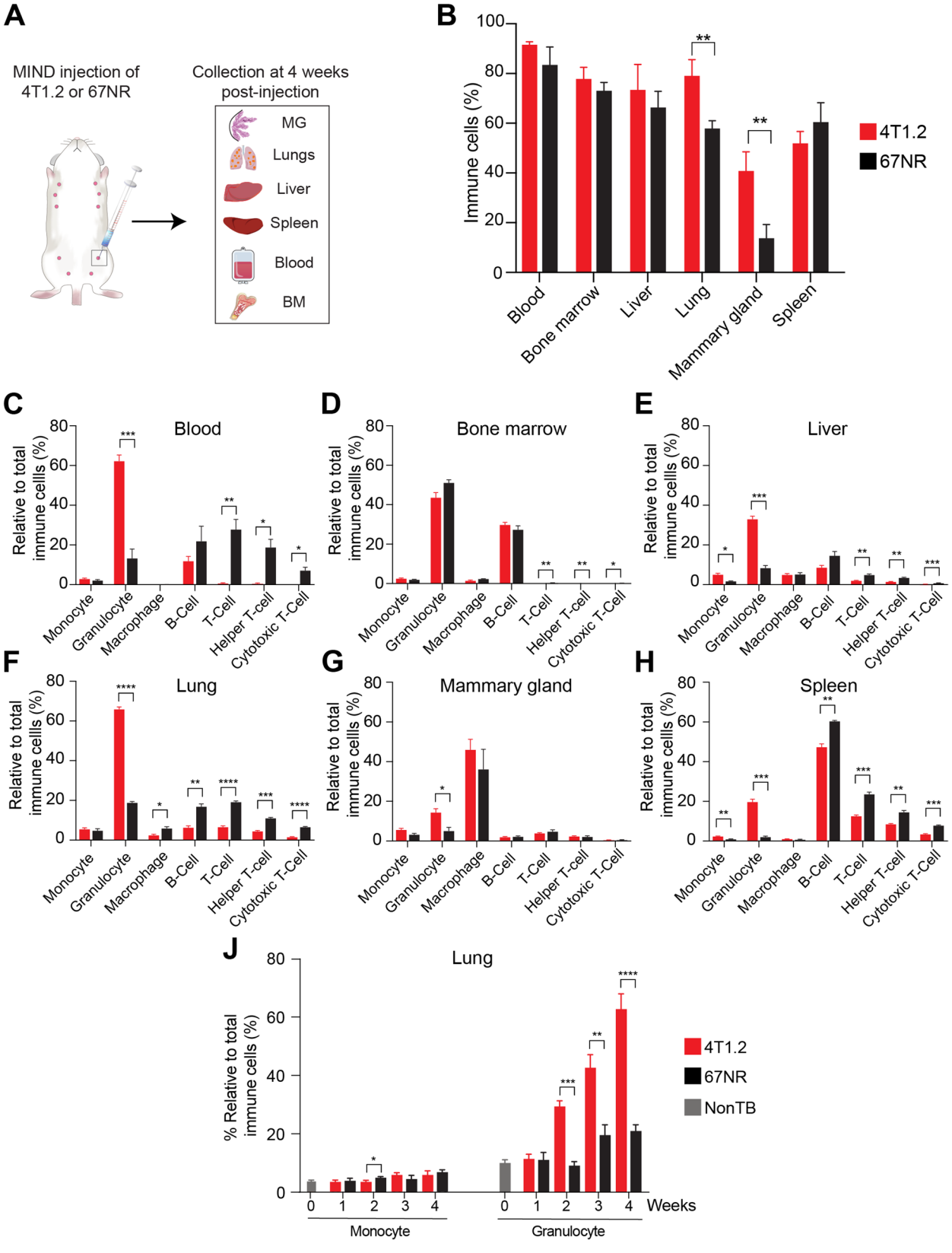

Fig. 4 (See legend on next page.)

(See figure on previous page.)

Fig. 4 Immune profiling of various organs of 4T1.2 or 67NR MIND tumour-bearing mice. **A** Schematic of collected organs for immune profiling. **B** Total proportion of the immune compartment (CD45 +) in blood, BM, liver, mammary gland and spleen. Percentages are relative to all live cells. Characterisation of immune populations in **C** blood, **D** bone marrow, **E** liver, **F** lung, **G** mammary gland, **H** spleen in both 4T1.2 and 67NR tumour-bearing mice. **J** proportions of monocytes and granulocytic cell populations during tumour development in lungs of 67NR and 4T1.2 tumour bearing MIND mice, Non TB (non-tumour bearing-mice). All statistical tests were performed with a student's t-test, with a minimum replicate size of n = 3 per group. (*p < 0.05, **p < 0.01, ***p < 0.001)

67NR fat pad model were significantly reduced compared with the 4T1.2 model. The proportion of granulocytes (CD45 + / CD11b + / Ly6G +) at week 2 post-implantation is higher in 4T1.2 than in 67NR tumours (Fig. 3E). However, there were no significant differences across models from week 2. Tumours also showed a steady increase in macrophages (CD45 + / CD11b + / F4/80 +) over time across all models (Fig. 3F). On the contrary, lymphoid infiltration of B-cells and T-cells was considerably reduced across all models, with decreasing populations observed as early as week 1 (Fig. 3G–H), but not significantly different between models and injection modes.

The analysis of the mammary tumour cell composition showed no major changes in immune infiltration but increased proportions of stromal cells in the intraductal model, particularly at the early stages of tumour initiation/progression. The higher proportion of stromal cells is consistent with the histology shown in Fig. 1A and a higher area of invasive edge (Fig. 2B). Together, these findings indicate that the intraductal model better preserves the tissue microenvironment during tumour formation and potentially suggests a better representation of interactions between cancer cells and the stroma.

Metastatic TNBC shows increased systemic proportions of myeloid cells and a reduced number of lymphocytes

The observed splenomegaly associated with metastasis indicated the presence of systemic inflammation in the 4T1.2 model (Fig. 2G). To further characterise this systemic inflammation, we extended the analysis of the immune profile to multiple sites (Fig. 4): blood, bone marrow, liver, lung, mammary gland, and spleen (Fig. 4A). Since the intraductal model was shown to better recapitulate tumour development, we focused on the 4T1.2 and 67NR intraductal models at late stage (4 weeks post-implantation). We first determined the relative abundance of the total immune compartment in each organ (Fig. 4B) within the live cell population (DAPI negative). The metastatic 4T1.2 model showed a significantly higher immune infiltration than the non-metastatic 67NR model in the lungs and the contralateral mammary glands. Further analysis of the immune composition in each organ showed that 4T1.2 tumours induced a higher proportion of myeloid cells, and a lower proportion of lymphoid populations compared with the 67NR model, excluding the bone marrow (Fig. 4C–H). Most of the myeloid cells found in the 4T1.2 model were identified as granulocytes, while the prevalent lymphoid populations in tissues of the 67NR model were B-cells and T-cells, excluding the bone marrow and the mammary gland. Given the relevance of myeloid-derived suppressor cell populations in the metastatic dissemination of mammary cancer cells, and the dramatic increase in granulocytes observed in the metastatic lungs at week 4, we investigated the temporal accumulation of monocytes and granulocytes in the lungs during tumour development (Fig. 4J). Our results revealed a sustained accumulation of granulocytes, but not monocytes, in the lungs of 4T1.2 tumour-bearing mice. This dramatic increase in granulocytes was significantly different from the lungs of 67NR tumour-bearing mice from week 2 of tumour development, further demonstrating that the transient increase in granulocytes observed in 67NR tumours (Fig. 3E) did not translate to a systemic accumulation at metastatic sites.

These data indicate that immunomodulation during metastasis is not restricted to the primary tumours and metastatic sites, but systemic inflammation is at play. Importantly, the systemic inflammation associated with metastatic dissemination was heavily skewed towards myeloid cell infiltration, particularly granulocytes, also defined as G-MDSCs, to the detriment of adaptive immune cell populations including cytotoxic T-cells. This is consistent with the promotion of an immune-tolerant environment driven by innate immune cells concomitant with the development of metastasis.

Single-cell RNAseq uncovers functional diversity of the immune phenotype during metastasis

To provide insights into the functional diversity of the immune cell lineages during metastasis, we performed single-cell RNA-Seq on viable CD45 + sorted cells from tumours and lungs from the 4T1.2 model using the BD Rhapsody™ Immune Response Panel. This panel includes 397 oligos targeting genes for the major inflammatory cytokines and transcriptional markers of the different immune cell subpopulations. After doublet exclusion and filtering of low-quality cells (low content of genes and "empty" droplets), we recovered a total of 5,321 cells from the lungs and 4,289 cells from tumours that were subsequently integrated for downstream analysis.

Unsupervised clustering revealed 17 cell subpopulations (Supp. Fig. 5A) that were further annotated using Single R (Supp. Fig. 5B) and canonical markers (Supp.

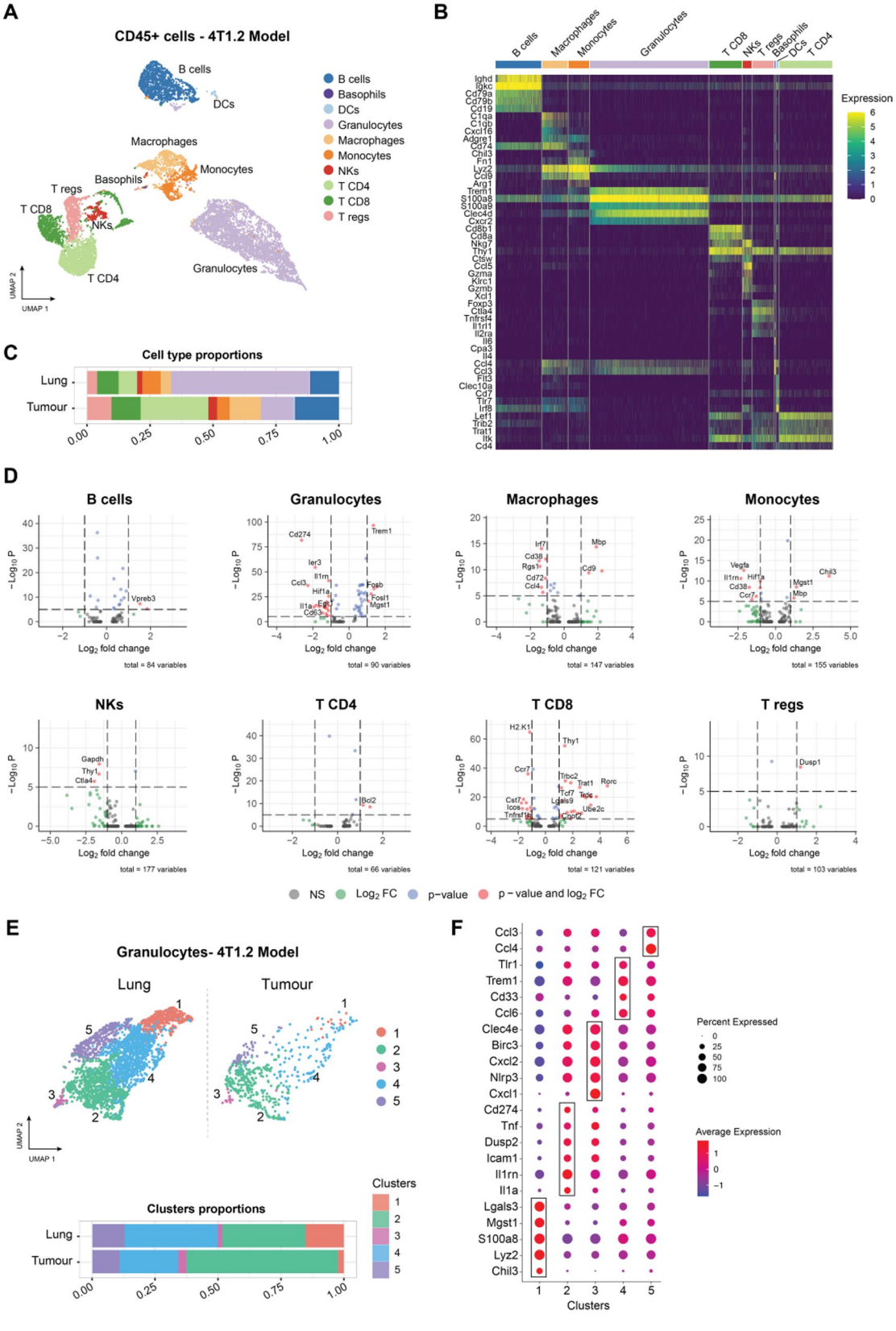

Fig. 5 (See legend on next page.)

(See figure on previous page.)

Fig. 5 Immune response atlas during TNBC metastasis. **A** UMAP visualisation of 9,610 integrated immune cells from tumours and lungs of the 4T1.2 mouse model at the 4-week timepoint. Cell types were annotated using SingleR signatures and canonical markers (Supp. Fig. 5). **B** Heatmap showing the differentially expressed genes (DEs) for each cell type. **C** Proportions of each cell type in the metastatic lung and primary tumour. **D** Enhanced volcano plots for each immune cell type showing the upregulated and downregulated genes in the lungs compared with tumours. The cut-off for log2 Fold Change (log2FC) is > 1, and the cut-off for P value is 1e−05. **E** UMAP visualisation of the granulocytic compartment in the lung and tumour of the 4T1.2 mouse model (Top). Proportions of each granulocytic cluster in the lung and tumour (bottom). **F** Dot plot showing the average gene expression across the granulocytic clusters. The size of the dot is determined by the percentage of cells expressing the given gene within a cluster

Fig. 5C and D) as B cells, basophils, dendritic cells (DCs), granulocytes, macrophages, monocytes, natural killer cells (NKs), T helper (T CD4), T cytotoxic (T CD8) and T regulatory (T regs) (Fig. 5A). The top markers defining each population are shown in Fig. 5B, the full list of markers can be found in Supp. Table 1. However, the proportions of cells varied between tissues (Fig. 5C). Consistent with our previous results, metastasis-impacted lungs contained a higher proportion of granulocytes, while the proportions of lymphocytes (specifically T regs, T CD4 and B cells) increased in the primary tumour. In addition to the changes in cell proportions, immune cell populations presented a different state of activation in the primary tumour and the metastatic sites. The most striking differences were found in myeloid cells and the T CD8 lymphocytes (Fig. 5D). Granulocytes in the lungs differentially expressed high levels of *Trem1*, a gene related to immunosuppression [53], and the transcription factors *Fosl1* and *Fosb* that regulate cell proliferation, differentiation and transformation [54]. In tumours, granulocytes differentially expressed *Cd274,* which encodes PD-L1. This immune checkpoint protein suppresses T-cell activation [55]. Tumour-infiltrated granulocytes also differentially expressed genes involved in angiogenesis, such as *Hif1a* [56], and genes encoding cytokines (*Ccl3*) and interleukins (*Il1rn* and *Il1a*) that are linked to innate inflammation [57, 58]. Macrophages and monocytes in the lungs upregulated the expression of the gene *Mbp*, an inflammatory activation marker [59, 60], and downregulated angiogenesis-related genes such as *Irf7*, *Vegfa* and *Hif1a*. Lastly, T CD8 cells in the metastatic lungs notably differed from primary tumour-infiltrated T CD8 cells, differentially expressing genes that regulate T cell activation, such as Thy1, *Ccr7* or *Icos* [61–63].

Given the relevance of the granulocytes in TNBC progression [47], we further characterised this cell lineage by sub-setting and re-clustering this population. We identified five subclasses of granulocytic subpopulations (Fig. 5E) with different infiltration patterns between the primary tumour and the metastatic lungs (Fig. 5E, bottom). The complete list of differential markers can be found in Supp. Table 2. The most noticeable distinction between tumours and lungs was the increased presence of cluster 1 and 4 in the metastatic lung with a lower representation of cluster 2. Differential gene expression analysis revealed the specific transcriptomic features of the granulocytic subpopulations (Fig. 5F). Clusters 2, 3, 4 and 5 share similarities in gene expression, whereas cluster 1 expresses genes that are exclusive and not shared with the other clusters. These specific genes for cluster 1 included *Lgals3*, *Mgst1*, *S100a8*, *Lyz2* and *Chil3*, which have been previously related to immunosuppression and metastatic spread [64–67], consistent with a granulocytic-MDSC phenotype. Together, these findings revealed different phenotypes and patterns of infiltration of granulocytes in primary tumours and at the metastatic site.

Discussion

TNBC still remains the breast cancer subtype with the worst prognosis, showing the highest rate of relapse [13]. The lack of specific targets in TNBC impedes effective and durable treatments. However, the revolutionary advancement of immunotherapy, especially immune checkpoint inhibitors (ICI), has provided a new avenue for targeted treatment in TNBC, showing improved survival rates and patient outcomes [19].

The intraductal model was first developed for the study of primary ductal carcinoma in situ (DCIS) [32, 35] and more recently it has been shown as a clinically relevant model for breast cancer progression and metastasis [26, 36]. In this study, we used two isogenic cell lines of mammary tumours—4T1.2 and 67NR, with differential metastatic capacity. These widely used models of TNBC were implanted either through a fat pad or an intraductal injection method. The advantage of intraductal injection of cancer cells through the teat and into the mammary duct is that it recapitulates the breast heterogeneity found during early tumorigenesis and models DCIS to invasive carcinoma [26, 32, 36]. This method of implantation permits a more natural progression of carcinoma within the ducts and invasion through the myoepithelial layer and basement membrane into the stroma (Fig. 2A). This stepwise development of the tumour by intraductal injection is more representative of human breast cancer as they primarily develop within the ductal tissue [32], compared to fat pad injections where cancer cells are inoculated in the mammary fat pad and external to the ducts. The histology, tumour development, and metastatic properties of fat pad injections of cancer cells are well characterised [68–70]; however, intraductal models are less frequently reported. Our data show that the intraductal model results in higher kinetics in tumour growth, endpoint tumour mass, and consistent with previous reports, higher metastatic burden compared to the conventional

fat pad model, presumably favoured by a higher proportion of invasive edge at early stages of tumour formation in the intraductal model. Increased metastatic burden is consistent with other reports in the 4T1.2 [25] and other xenografts of human cell lines in immunocompromised mice [34]. We determined that hypoxic areas in the tumours correlated with intense apoptosis, however this was not a differential factor between the models, but a factor directly related to tumour size (Supp. Fig. 3).

We have also observed that both the fat pad and intraductal models show a similar immune composition as the tumour develops and during metastasis. The most substantial changes occurred qualitatively in the systemic inflammation between the 4T1.2 and 67NR models: specifically, the infiltration of granulocytes in metastatic lungs (Fig. 4F). In an inflammatory and pathological context such as cancer, tumour-infiltrated granulocytes promote tumour progression and dissemination through various mechanisms, such as creating an immunosuppressive microenvironment by suppressing T-cell activity [71, 72], promoting epithelial-to-mesenchymal (EMT) transition [73], remodifying the ECM [74], and creating the pre-metastatic niche [73]. Interestingly, compared with 4T1.2 fat pad tumours, 67NR fat pad tumours present a transient increase of granulocytes at week 1 post implantation, however this is not subsequently sustained or translated into systemic inflammation, and together with limited ECM interactions [40], results in an impaired development of metastasis. Consistent with our earlier study [47], we observed an increase in the granulocytic population within the lungs of the 4T1.2-tumour bearing mice at week 2 and further increases by week 4 (Fig. 5). Ghosh and colleagues reported that metastasis has been observed in the 4T1 intraductal model as early as 2 weeks [26], indicating that the increase in the granulocytic population observed at 2 weeks is promoting the early development of the pre-metastatic niche. Granulocytic cells, including granulocytic MDSCs (G-MDSCs), have been observed to be systemically mobilised and accumulated within the lungs before the deposition of cancer cells [75–77]. Targeting granulocytic MDSCs has been shown to reduce metastatic dissemination in breast cancer and other cancer types [42, 78, 79]. Interestingly, the injection method did not affect the granulocytic infiltration into the lungs, however, the intraductal 4T1.2 tumours caused a significantly higher level of metastasis burden compared to the fat pad 4T1.2 at 4 weeks after cancer cell implantation (Fig. 2F). Since the metastatic phenotype is regulated by various factors from the TME, it is likely the intraductal injection propagates a more malignant phenotype that is exacerbated by the ductal epithelial microenvironment and stroma providing more opportunities for escape [25, 80]. Intraductal tumours have a proportionally larger area of invasive edge at early timepoints, which might result in higher occurrence of Tumour Microenvironment of Metastasis doorways, and favoured with a highly myeloid cell infiltration might confer a metastatic advantage [81]. Despite increased inflammation, it has been proposed that the impaired metastatic potential of 67NR may be due to other factors [40].

Dissecting the role of immune cells is key to understanding the disparity observed in successful clinical response to therapy [82, 83]. Not surprisingly, the immune system relies on a sensitive balance between lymphoid and myeloid cells. However, in cancer, tumour cells can exploit the immune system through amplified myelopoiesis resulting in a reciprocal reduction of lymphoid cells and their function. The expansion of dysfunctional myeloid cells can co-evolve with the tumour to promote an inflammatory and immunosuppressive TME to facilitate tumour growth and dissemination [82]. As such, high counts of circulating myeloid cells, in particular neutrophils and G-MDSCs, and elevated neutrophil-to-lymphocyte ratios have been correlated with tumour progression and are associated with poor prognosis [84, 85]. Although the lungs are a typical metastatic site in breast cancer we found that granulocytes are expanded systemically across all organs in 4T1.2 tumour-bearing mice, except for bone marrow. This indicates that G-MDSC trafficking is not restricted to the tumour and metastatic sites but also to other distal organs. This is in line with previous reports from both PyMT and 4T1 models [75, 78].

A higher myeloid immune infiltrate is associated with poorer prognosis, increased metastasis, and resistance to immune checkpoint therapy [17, 86–88]. Correlations between MDSC recruitment and their role in creating a pre-metastatic niche and promoting metastasis to secondary organs have been well established [42, 73, 89]. Our previous study using the transgenic MMTV-PyMT mice has also demonstrated the importance of MDSC infiltration in promoting tumour progression, metastasis, and vascularity [42]. Cao, Y et al. and others have shown that MDSCs extracted from lungs and spleens of mice bearing 4T1 tumours are capable of inhibiting T-cell proliferation in a dose-dependent manner, whereas MDSCs from 67NR had much lower immunosuppressive capacity [78, 90]. In addition, previous reports suggested that signalling factors, such as G-CSF, derived from 4T1 cells within the mammary duct shift the polarisation of myeloid cells to create a pro-metastatic TME via the recruitment of MDSCs [78, 90, 91]. However, given the heterogeneous nature of MDSCs, these studies only identify the main myeloid lineages (monocytic and granulocytic), and, as a consequence, they do not distinguish between subpopulations and cell states. To overcome this limitation, we leveraged targeted scRNAseq technology

to provide a high-resolution molecular atlas of the differences in the immune cell lineages in mammary tumours and lung metastasis (Fig. 5). This high-resolution map uncovered the transcriptional differences among immune cells depending on their spatial distribution, with granulocytes from cluster 1 predominantly present in the metastatic lungs. Top differential marker genes expressed by cluster 1 granulocytes (*Lgals3, S100A8, Lyz2 and Chil3*) are present in a gene signature of granulocytic MDSCs previously defined by single cell RNAseq in Lewis-Lung Carcinoma (LLC) [67]. These top marker genes are related to immunosuppressive and pro-metastatic functions of MDSCs. Galectin-3 encoded by the gene *Lgals3* is a modulator of the pro-metastatic function of MDSCs in cervical cancer [92]. The chitinase-like protein encoded by Chil3 has recently been found to be a key marker of $CD115^{-}$ MDSCs which are precursors of granulocytic MDSCs [93]. The expression of the ferroptosis-associated Mgst1 gene has been found correlated with MDSCs in endometrial carcinoma [65] and has been reported to be a MDSC marker in breast cancer [94]. Our results provide further evidence for modelling MDSCs during metastasis development using the 4T1.2 model, opening new avenues to characterise the functional activation and heterogeneity of MDSCs.

Intraductal syngeneic models can be used to study the development of TNBC in a immunocompetent scenario, however there are limitations to these models. Firstly, the rapid development of the transplanted tumours does not recapitulate the appropriate kinetics of human breast cancer compared to genetically engineered mouse models [95]. Secondly, inflammatory processes associated with cell implantation might trigger wound healing processes that are independent of the inherent carcinogenic process. Finally, as these models use a murine immune system, their translatability to the human context must be appropriately framed, especially for drug development and immunotherapeutic targets. These limitations are inherent in all syngeneic mouse models. In our study, 67NR cells formed tumours that grew faster than 4T1.2 tumours, despite starting with fewer injected cells. This was not observed previously [47] but subsequent syngeneic model studies have reported variable kinetics of tumour formation between cell lines [36], with cancer cell concentration and viability at the time of injection [36], as well as selection pressure during culture conditions [80], as factors influencing growth kinetics, even within the same cell line.

To our knowledge, this is the first systematic immune cell profiling of 4T1.2 and 67NR intraductal tumours. It also provides a high-resolution landscape of immune activation in the microenvironment of tumours and metastatic lungs. We envision that this study will contribute to the toolbox for modelling the role of the immune system in metastatic dissemination. It will also guide further mechanistic studies to develop new immunotherapeutics and biomarkers for immunosuppressive myeloid populations, and to understand their effects on effector immune cells. With the acceleration of single-cell resolution multiomic technology, understanding the contribution of other cell lineages will shed new light on the multicellular processes that drive metastasis.

Conclusions

Our study demonstrated that intraductal implantation of mouse mammary cancer cells better represents the early stages of tumour formation, indicating a more valid recapitulation of cellular and molecular communication between cancer cells and the tissue microenvironment. We delineated the differential inflammation between metastatic and non-metastatic scenarios both systemically and specifically at the tumour and metastatic sites. Metastatic inflammation was characterised by widespread G-MDSCs expansion and reduced lymphocyte representation. Qualitatively, the immune activation of G-MDCSs, monocytes and lymphocytes was remarkably different between the primary tumour and the metastatic site, highlighting heterogeneous immune functions with potential implications for the design of anticancer strategies based on immunomodulation.

Overall, this study shows that the intraductal model is superior for investigating breast cancer progression and the associated immune response, providing valuable insights into tumour biology and therapeutic strategies.

Supplementary Information

The online version contains supplementary material available at https://doi.org/10.1186/s13058-025-02186-4.

Supplementary Material 1. Fig 1. Representative gating strategy for immune characterisation. Representative gating strategy used in FACS with canonical surface markers used to identify major cell populations. Primary tumour A) and lungs B) of 4-week 4T1.2 intraductal model was used as an example. Canonical markers used to identify the specific populations are also shown (bottom).

Supplementary Material 2. Fig 2. Histopathological and metastatic burden comparison of tumour progression between conventional orthotopic and MIND injection. A) Representative workflow of invasive area quantification. The boxed regions in yellow are enlarged in the right panels. Invasive areas were identified as the area of the tumour edge intercalating with normal tissue (arrows). Tumour (pink) and invasive (cyan) areas were marked and quantified (scale bars, 1000 and 200μm). B, top) Representative images of Picrosirius red at 2 weeks. The boxed regions are enlarged in the bottom panels (scale bar, 200μm). B, bottom) Magnification of the highlighted area in yellow. Arrows show the Picrosirius red staining (scale bar, 50μm). C) Quantification over 4 weeks of Picrosirius red staining. F, left) Representative images and H&E of lungs at 4 weeks post-injection. D) Histogram showing the number of metastases in the lungs at week 4. E) Violin plot showing the area of individual metastasis. All statistical tests were performed with a student's t-test with at least n=3 replicates per group.

Supplementary Material 3. Fig 3. Histological analysis of hypoxia in 4T1.2 and 67NR MIND and fat pad tumours. A) Representative images of KI67, CC3 and GLUT1 distribution over 4 weeks (scale bar, 100μm). B) Quantification over 4 weeks of the percentage of the tumour area showing a

strong signal for GLUT1. C) Dot plot and Pearson correlation between the percentage of strong GLUT1 signal and the total area of tumour. Statistical tests were performed with One-way ANOVA and post hoc Tukey. ¤ = significance between 4T1.2 orthotopic and 4T1.2 MIND; † = significance between 67NR orthotopic and 4T1.2 orthotopic. Data is presented as means ± SD. ($p< 0.05$).

Supplementary Material 4. Fig 4. Histological analysis of tumour stroma of 4T1.2 and 67NR MIND and fat pat tumours. A) Representative images of harvested tumours at 1 week stained for PanCK, α-SMA and nuclei (scale bar, 50μm). B) Histogram representing the number of positive cells for α-SMA in the tumour area. Statistical test was performed with One-way ANOVA and post hoc Tukey. Data is presented as means ± SD. ($p< 0.05$).

Supplementary Material 5. Fig 5. Identification of the major immune cell types involved in TNBC metastasis. A) Uniform Manifold Approximation and Projection (UMAP) visualisation of unsupervised cell clustering of the integrated scRNAseq datasets of tumours and lungs from the 4T1.2 mouse model. B) Heatmap showing SingleR signatures for each unsupervised cluster in A. SingleR signatures are based on the mouse cell type reference generated by the Immunologic Genome Project [46]. C and D) Feature plots showing the expression of canonical markers for C) natural killer cells (NKs) and D) T cells. Cd4 identifies T helper (T CD4), Cd8a T cytotoxic (T CD8) and Foxp3 T regulatory (T regs).

Supplementary Material 6. Table 1. Marker gene list for the leukocyte clusters in Figure 5A by cell type. Markers are generated using the "FindAllMarkers" in the Seurat package for single-cell RNAseq analysis.

Supplementary Material 7. Table 2. Marker gene list for the granulocyte clusters in Figure 5E. Markers are generated using the "FindAllMarkers" in the Seurat package for single-cell RNAseq analysis.

Acknowledgements
We thank the members of the Functional Genomics Laboratory at School of Biomedical Engineering in the Faculty of Engineering and Information Technology (University of Technology Sydney) and the Cancer Epigenetics Biology and Therapeutics group at Children's Cancer Institute (University of New South Wales) for helpful discussions. The authors gratefully acknowledge the Microbial Imaging Facility (University of Technology Sydney) for their support and assistance in this work. We also thank and acknowledge The Garvan Institute's Histopathology and Biospecimen, and especially Anaiis Zaratzian, Andrew Da Silva, and Michael Tayao, for their support and services (tissue processing, sectioning, H&E staining and Immunohistochemistry optimisation and staining) provided for our project. JV current affiliation: Department of Laboratory Medicine, Laboratory of Hematology, Radboud University Medical Center, Research Institute for Medical Innovation, Nijmegen, The Netherlands.

Author contributions
L.R.F, A.M.K.L, F.V.M and D.G.O were involved in the experimental conceptualisation and design; L.R.F, A.M.K.L, L.R.S, F.S, and L.C performed the experimental work and data acquisition; L.R.F, A.M.K.L, L.R.S and J.V conducted data analysis and original draft preparation; R.L.A provided resource, intellectual input and reviewed the manuscript; L.R.F, L.R.S, F.V.M, and D.G.O wrote, reviewed and edited the manuscript.

Funding
A.M.K.L. was supported by a UPA Scholarship from UNSW This work was supported by the National Breast Cancer Foundation (IIRS21-096, Elaine Henry Fellowship and IIRS21-068), Cancer Institute NSW Career Development Fellowship (DG00625) and Cancer Council NSW project grants (RG18-03) and (RG23-09) to DGO; a Cancer Institute NSW Career Development Fellowship (2019-2021, CDF181218) to FVM; and the Australian Government Research Training Program (RTP) Scholarship to AMKL.

Data availability
The datasets generated during and/or analysed during the current study are available in the Gene Expression Omnibus (GEO) database repository under the following number (*this provided upon acceptance of the manuscript*). uploads/emma.ronca@orcid_0ZWx2Mce/67NR_4T1_MDSCs_GEO_sub.

Declarations

Ethics approval and consent to participate
Animals used in this article were approved under the St. Vincent's Hospital Animal Ethics Committee (AEC) #17/23 and #19/02.

Consent for publication
Not applicable.

Competing interests
The authors declare no competing interests.

Author details
[1]Faculty of Engineering and IT, School of Biomedical Engineering, University of Technology Sydney, Ultimo, NSW, Australia
[2]Cancer Epigenetic Biology and Therapeutics, Precision Medicine, Children's Cancer Institute, Kensington, NSW, Australia
[3]The Kinghorn Cancer Centre, Garvan Institute of Medical Research, Darlinghurst, NSW, Australia
[4]Olivia Newton-John Cancer Research Institute, Heidelberg, VIC, Australia
[5]School of Cancer Medicine, La Trobe University, Bundoora, VIC, Australia
[6]Department of Clinical Pathology, The University of Melbourne, Melbourne, VIC, Australia
[7]School of Clinical Medicine. Faculty of Medicine, University of New South Wales Sydney, Sydney, NSW, Australia

Received: 11 April 2025 / Accepted: 24 November 2025
Published online: 10 December 2025

References

1. Sung H, et al. Global cancer statistics 2020: GLOBOCAN estimates of incidence and mortality worldwide for 36 cancers in 185 countries. CA Cancer J Clin. 2021;71(3):209–49.
2. Siegel RL, et al. Cancer statistics, 2021. CA Cancer J Clin. 2021;71(1):7–33.
3. Giaquinto AN, et al. Breast cancer statistics, 2022. CA Cancer J Clin. 2022;72(6):524–41.
4. Cortes J, et al. Pembrolizumab plus chemotherapy in advanced triple-negative breast cancer. N Engl J Med. 2022;387(3):217–26.
5. van den Ende NS, et al. Triple-negative breast cancer and predictive markers of response to neoadjuvant chemotherapy: a systematic review. Int J Mol Sci. 2023. https://doi.org/10.3390/ijms24032969.
6. Mittendorf EA, et al. Neoadjuvant atezolizumab in combination with sequential nab-paclitaxel and anthracycline-based chemotherapy versus placebo and chemotherapy in patients with early-stage triple-negative breast cancer (IMpassion031): a randomised, double-blind, phase 3 trial. Lancet. 2020;396(10257):1090–100.
7. da Silva JL, et al. Cancer immunotherapy: the art of targeting the tumor immune microenvironment. Cancer Chemother Pharmacol. 2019;84(2):227–40.
8. Ladoire S, et al. In situ immune response after neoadjuvant chemotherapy for breast cancer predicts survival. J Pathol. 2011;224(3):389–400.
9. Ruffell B, et al. Leukocyte composition of human breast cancer. Proc Natl Acad Sci USA. 2012;109(8):2796–801.
10. Denkert C, et al. Tumor-associated lymphocytes as an independent predictor of response to neoadjuvant chemotherapy in breast cancer. J Clin Oncol. 2010;28(1):105–13.
11. Schmidt M, et al. The humoral immune system has a key prognostic impact in node-negative breast cancer. Cancer Res. 2008;68(13):5405–13.
12. Loi S, et al. Prognostic and predictive value of tumor-infiltrating lymphocytes in a phase III randomized adjuvant breast cancer trial in node-positive breast cancer comparing the addition of docetaxel to doxorubicin with doxorubicin-based chemotherapy: BIG 02–98. J Clin Oncol. 2013;31(7):860–7.
13. Vikas P, Borcherding N, Zhang W. The clinical promise of immunotherapy in triple-negative breast cancer. Cancer Manag Res. 2018;10:6823–33.
14. Law AMK, et al. Advancements in 3D cell culture systems for personalizing anti-cancer therapies. Front Oncol. 2021;11:782766.
15. Mahmoud SM, et al. Tumor-infiltrating CD8+ lymphocytes predict clinical outcome in breast cancer. J Clin Oncol. 2011;29(15):1949–55.
16. Shang B, et al. Prognostic value of tumor-infiltrating FoxP3+ regulatory T cells in cancers: a systematic review and meta-analysis. Sci Rep. 2015;5:15179.

17. Zhang S, et al. The role of myeloid-derived suppressor cells in patients with solid tumors: a meta-analysis. PLoS ONE. 2016;11(10):e0164514.
18. Li F, et al. Tumor-infiltrating Treg, MDSC, and IDO expression associated with outcomes of neoadjuvant chemotherapy of breast cancer. Cancer Biol Ther. 2018;19(8):695–705.
19. Rayson VC, et al. The anti-cancer immune response in breast cancer: current and emerging biomarkers and treatments. Trends Cancer. 2024. https://doi.org/10.1016/j.trecan.2024.02.008.
20. Schmid P, et al. Pembrolizumab for early triple-negative breast cancer. N Engl J Med. 2020;382(9):810–21.
21. Dobosz P, et al. Challenges of the immunotherapy: perspectives and limitations of the immune checkpoint inhibitor treatment. Int J Mol Sci. 2022. https://doi.org/10.3390/ijms23052847.
22. Ventola CL. Cancer immunotherapy, part 3: challenges and future trends. P T. 2017;42(8):514–21.
23. Winer EP, et al. Pembrolizumab versus investigator-choice chemotherapy for metastatic triple-negative breast cancer (KEYNOTE-119): a randomised, open-label, phase 3 trial. Lancet Oncol. 2021;22(4):499–511.
24. Leach DR, Krummel MF, Allison JP. Enhancement of antitumor immunity by CTLA-4 blockade. Science. 1996;271(5256):1734–6.
25. Atiya HI, et al. Intraductal adaptation of the 4T1 mouse model of breast cancer reveals effects of the epithelial microenvironment on tumor progression and metastasis. Anticancer Res. 2019;39(5):2277–87.
26. Ghosh A, et al. MIND model for triple-negative breast cancer in syngeneic mice for quick and sequential progression analysis of lung metastasis. PLoS ONE. 2018;13(5):e0198143.
27. Zhang Y, et al. Establishment of a murine breast tumor model by subcutaneous or orthotopic implantation. Oncol Lett. 2018;15(5):6233–40.
28. Zhao X, et al. Tumor location impacts immune response in mouse models of colon cancer. Oncotarget. 2017;8(33):54775–87.
29. Yu JW, et al. Tumor-immune profiling of murine syngeneic tumor models as a framework to guide mechanistic studies and predict therapy response in distinct tumor microenvironments. PLoS ONE. 2018;13(11):e0206223.
30. Nakano K, et al. Difference in morphology and interactome profiles between orthotopic and subcutaneous gastric cancer xenograft models. J Toxicol Pathol. 2018;31(4):293–300.
31. Zhang W, et al. Comparative study of subcutaneous and orthotopic mouse models of prostate cancer: vascular perfusion, vasculature density, hypoxic burden and BB2r-targeting efficacy. Sci Rep. 2019;9(1):11117.
32. Behbod F, et al. An intraductal human-in-mouse transplantation model mimics the subtypes of ductal carcinoma in situ. Breast Cancer Res. 2009;11(5):R66.
33. Fiche M, et al. Intraductal patient-derived xenografts of estrogen receptor alpha-positive breast cancer recapitulate the histopathological spectrum and metastatic potential of human lesions. J Pathol. 2019;247(3):287–92.
34. Young AI, et al. MCL-1 inhibition provides a new way to suppress breast cancer metastasis and increase sensitivity to dasatinib. Breast Cancer Res. 2016;18(1):125.
35. Valdez KE, et al. Human primary ductal carcinoma in situ (DCIS) subtype-specific pathology is preserved in a mouse intraductal (MIND) xenograft model. J Pathol. 2011;225(4):565–73.
36. Bernhardt SM, et al. Isogenic mammary models of intraductal carcinoma reveal progression to invasiveness in the absence of a non-obligatory in situ stage. Cancers. 2023. https://doi.org/10.3390/cancers15082257.
37. Nguyen, D.-A., et al., *Intraductal Injection into the mouse mammary gland*, in *methods in mammary gland biology and breast cancer research*, M.M. Ip and B.B. Asch, Editors. 2000, Springer US: Boston, MA. pp. 259–270.
38. Aslakson CJ, Miller FR. Selective events in the metastatic process defined by analysis of the sequential dissemination of subpopulations of a mouse mammary tumor. Cancer Res. 1992;52(6):1399–405.
39. Lelekakis M, et al. A novel orthotopic model of breast cancer metastasis to bone. Clin Exp Metastasis. 1999;17(2):163–70.
40. Eckhardt BL, et al. Genomic analysis of a spontaneous model of breast cancer metastasis to bone reveals a role for the extracellular matrix. Mol Cancer Res. 2005;3(1):1–13.
41. de la Rodriguez Fuente L, et al. Tumor dissociation of highly viable cell suspensions for single-cell omic analyses in mouse models of breast cancer. STAR Protoc. 2021;2(4):100841.
42. Gallego-Ortega D, et al. ELF5 drives lung metastasis in luminal breast cancer through recruitment of Gr1+ CD11b+ myeloid-derived suppressor cells. PLoS Biol. 2015;13(12):e1002330.
43. Law AMK, et al. Andy's algorithms: new automated digital image analysis pipelines for FIJI. Sci Rep. 2017;7(1):15717.
44. Hao Y, et al. Integrated analysis of multimodal single-cell data. Cell. 2021;184(13):3573–87.
45. Aran D, et al. Reference-based analysis of lung single-cell sequencing reveals a transitional profibrotic macrophage. Nat Immunol. 2019;20(2):163–72.
46. Heng TS, Painter MW, C. Immunological Genome Project. The immunological genome project: networks of gene expression in immune cells. Nat Immunol. 2008;9(10):1091–4.
47. Swierczak A, et al. The promotion of breast cancer metastasis caused by inhibition of CSF-1R/CSF-1 signaling is blocked by targeting the G-CSF receptor. Cancer Immunol Res. 2014;2(8):765–76.
48. Wellberg EA, et al. The glucose transporter GLUT1 is required for ErbB2-induced mammary tumorigenesis. Breast Cancer Res. 2016;18(1):131.
49. Neophytou CM, et al. The role of tumor microenvironment in cancer metastasis: molecular mechanisms and therapeutic opportunities. Cancers. 2021. https://doi.org/10.3390/cancers13092053.
50. Valdes-Mora F, et al. Single-cell transcriptomics reveals involution mimicry during the specification of the basal breast cancer subtype. Cell Rep. 2021;35(2):108945.
51. Law AMK, Valdes-Mora F, Gallego-Ortega D. Myeloid-derived suppressor cells as a therapeutic target for cancer. Cells. 2020. https://doi.org/10.3390/cells9030561.
52. DuPre SA, Hunter KW Jr. Murine mammary carcinoma 4T1 induces a leukemoid reaction with splenomegaly: association with tumor-derived growth factors. Exp Mol Pathol. 2007;82(1):12–24.
53. Wu Q, et al. Blocking triggering receptor expressed on myeloid cells-1-positive tumor-associated macrophages induced by hypoxia reverses immunosuppression and anti-programmed cell death ligand 1 resistance in liver cancer. Hepatology. 2019;70(1):198–214.
54. Jiang X, et al. Expression and function of FRA1 protein in tumors. Mol Biol Rep. 2020;47(1):737–52.
55. Zuazo M, et al. Molecular mechanisms of programmed cell death-1 dependent T cell suppression: relevance for immunotherapy. Ann Transl Med. 2017;5(19):385.
56. Cimmino F, et al. HIF-1 transcription activity: HIF1A driven response in normoxia and in hypoxia. BMC Med Genet. 2019;20(1):37.
57. Dinarello CA. Overview of the IL-1 family in innate inflammation and acquired immunity. Immunol Rev. 2018;281(1):8–27.
58. Zhao H, et al. Inflammation and tumor progression: signaling pathways and targeted intervention. Signal Transduct Target Ther. 2021;6(1):263.
59. Feng JM. Minireview: expression and function of golli protein in immune system. Neurochem Res. 2007;32(2):273–8.
60. Shiryaev SA, et al. Inflammatory proprotein convertase-matrix metalloproteinase proteolytic pathway in antigen-presenting cells as a step to autoimmune multiple sclerosis. J Biol Chem. 2009;284(44):30615–26.
61. Unsoeld H, et al. Cutting edge: CCR7+ and CCR7- memory T cells do not differ in immediate effector cell function. J Immunol. 2002;169(2):638–41.
62. Peng C, et al. Engagement of the costimulatory molecule ICOS in tissues promotes establishment of CD8(+) tissue-resident memory T cells. Immunity. 2022;55(1):98–114.
63. Gunter KC, et al. Thy-1-mediated T-cell activation requires co-expression of CD3/Ti complex. Nature. 1987;326(6112):505–7.
64. Ahmed H, AlSadek DM. Galectin-3 as a potential target to prevent cancer metastasis. Clin Med Insights Oncol. 2015;9:113–21.
65. Yan J, Ye G, Shao Y. High expression of the ferroptosis-associated MGST1 gene in relation to poor outcome and maladjusted immune cell infiltration in uterine corpus endometrial carcinoma. J Clin Lab Anal. 2022;36(4):e24317.
66. Basso D, Fogar P, Plebani M. The S100A8/A9 complex reduces CTLA4 expression by immature myeloid cells: implications for pancreatic cancer-driven immunosuppression. Oncoimmunology. 2013;2(6):e24441.
67. Veglia F, et al. Analysis of classical neutrophils and polymorphonuclear myeloid-derived suppressor cells in cancer patients and tumor-bearing mice. J Exp Med. 2021. https://doi.org/10.1084/jem.20201803.
68. Tabaries S, et al. Granulocytic immune infiltrates are essential for the efficient formation of breast cancer liver metastases. Breast Cancer Res. 2015;17:45.
69. Bailey-Downs LC, et al. Development and characterization of a preclinical model of breast cancer lung micrometastatic to macrometastatic progression. PLoS ONE. 2014;9(5):e98624.
70. Paschall AV, Liu K. An orthotopic mouse model of spontaneous breast cancer metastasis. J Visual Exp JoVE. 2016;114:54040.

71. Bronte V, Zanovello P. Regulation of immune responses by L-arginine metabolism. Nat Rev Immunol. 2005;5(8):641–54.
72. Gabrilovich DI, Nagaraj S. Myeloid-derived suppressor cells as regulators of the immune system. Nat Rev Immunol. 2009;9(3):162–74.
73. Condamine T, et al. Regulation of tumor metastasis by myeloid-derived suppressor cells. Annu Rev Med. 2015;66:97–110.
74. Yan HH, et al. Gr-1+CD11b+ myeloid cells tip the balance of immune protection to tumor promotion in the premetastatic lung. Cancer Res. 2010;70(15):6139–49.
75. Wculek SK, Malanchi I. Neutrophils support lung colonization of metastasis-initiating breast cancer cells. Nature. 2015;528(7582):413–7.
76. Coffelt SB, et al. IL-17-producing gammadelta T cells and neutrophils conspire to promote breast cancer metastasis. Nature. 2015;522(7556):345–8.
77. Ya G, et al. Role of myeloid-derived suppressor cells in the formation of pre-metastatic niche. Front Oncol. 2022;12:975261.
78. Bosiljcic M, et al. Targeting myeloid-derived suppressor cells in combination with primary mammary tumor resection reduces metastatic growth in the lungs. Breast Cancer Res. 2019;21(1):103.
79. Banuelos A, et al. CXCR2 inhibition in G-MDSCs enhances CD47 blockade for melanoma tumor cell clearance. Proc Natl Acad Sci USA. 2024;121(5):e2318534121.
80. Sflomos G, et al. A preclinical model for ERalpha-positive breast cancer points to the epithelial microenvironment as determinant of luminal phenotype and hormone response. Cancer Cell. 2016;29(3):407–22.
81. Ginter PS, et al. Tumor microenvironment of metastasis (TMEM) doorways are restricted to the blood vessel endothelium in both primary breast cancers and their lymph node metastases. Cancers. 2019. https://doi.org/10.3390/cancers11101507.
82. Law AM, et al. The innate and adaptive infiltrating immune systems as targets for breast cancer immunotherapy. Endocr Relat Cancer. 2017;24(4):R123–44.
83. Binnewies M, et al. Understanding the tumor immune microenvironment (TIME) for effective therapy. Nat Med. 2018;24(5):541–50.
84. Wu WC, et al. Circulating hematopoietic stem and progenitor cells are myeloid-biased in cancer patients. Proc Natl Acad Sci USA. 2014;111(11):4221–6.
85. Jung MR, et al. Elevated preoperative neutrophil to lymphocyte ratio predicts poor survival following resection in late stage gastric cancer. J Surg Oncol. 2011;104(5):504–10.
86. Mouchemore KA, Anderson RL. Immunomodulatory effects of G-CSF in cancer: therapeutic implications. Semin Immunol. 2021;54:101512.
87. Bjoern J, et al. Immunological correlates of treatment and response in stage IV malignant melanoma patients treated with Ipilimumab. Oncoimmunology. 2016;5(4):e1100788.
88. Meyer C, et al. Frequencies of circulating MDSC correlate with clinical outcome of melanoma patients treated with ipilimumab. Cancer Immunol Immunother. 2014;63(3):247–57.
89. Wang Y, et al. MDSCs: key criminals of tumor pre-metastatic niche formation. Front Immunol. 2019;10:172.
90. Cao Y, et al. BMP4 inhibits breast cancer metastasis by blocking myeloid-derived suppressor cell activity. Cancer Res. 2014;74(18):5091–102.
91. Steenbrugge J, et al. Anti-inflammatory signaling by mammary tumor cells mediates prometastatic macrophage polarization in an innovative intraductal mouse model for triple-negative breast cancer. J Exp Clin Cancer Res. 2018;37(1):191.
92. Mai Q, et al. Galectin-3 suppresses CD8(+) T cells function via myeloid-derived suppressor cells recruitment in cervical cancer. Int J Biol Macromol. 2025;311(Pt 4):143683.
93. Zou Y, et al. CD115(–) monocytic myeloid-derived suppressor cells are precursors of OLFM4(high) polymorphonuclear myeloid-derived suppressor cells. Commun Biol. 2023;6(1):272.
94. Wang Q, et al. Single-cell profiling guided combinatorial immunotherapy for fast-evolving CDK4/6 inhibitor-resistant HER2-positive breast cancer. Nat Commun. 2019;10(1):3817.
95. DuPage M, Jacks T. Genetically engineered mouse models of cancer reveal new insights about the antitumor immune response. Curr Opin Immunol. 2013;25(2):192–9.

Publisher's Note